Effect of Pure Dephasing and Phonon Scattering on the Coupling of Semiconductor Quantum Dots to Optical Cavities

C. Jarlov,* É. Wodey, A. Lyasota, M. Calic, P. Gallo, B. Dwir, A. Rudra, and E. Kapon
Laboratory of Physics of Nanostructures, Ecole Polytechnique Fédérale de Lausanne (EPFL), CH-1015 Lausanne, Switzerland
(Received 4 May 2016; published 8 August 2016)

Using site-controlled semiconductor quantum dots (QDs) free of multiexcitonic continuum states, integrated with photonic crystal membrane cavities, we clarify the effects of pure dephasing and phonon scattering on exciton-cavity coupling in the weak-coupling regime. In particular, the observed QD-cavity copolarization and cavity mode feeding versus QD-cavity detuning are explained quantitatively by a model of a two-level system embedded in a solid-state environment.

DOI: 10.1103/PhysRevLett.117.076801

Investigations of cavity quantum electrodynamics (c-QED), initially carried out with atomic systems [1], have been extended to solid-state platforms such as superconducting circuits [2] and quantum dots (QDs) incorporated in photonic nanocavities [3]. Although the latter systems are more robust, hence offering a viable approach to quantum information technology [4,5], they are inherently susceptible to quantum decoherence induced by the solid-state environment. The most relevant dephasing processes in semiconductor QD systems are interactions with phonons [6] and pure dephasing due to electrically charged environment impurities [7] [Fig. 1(a)]. Previous studies of QD-cavity systems performed with self-assembled QDs evidenced the presence of spurious multiexcitonic effects [8,9], making difficult the unraveling of the impact of inherent dephasing processes on QD-cavity interaction. Here, we employ site-controlled pyramidal QDs, representing a near-ideal two-level system (TLS) free of spurious multiexcitonic effects [10,11], to elucidate the role of quantum decoherence on cavity mode (CM) feeding [12] and exciton emission copolarization [10,13] at finite CM-QD energy detuning. Based on a theoretical modeling of polarization-resolved photoluminescence (PL) spectra performed at the single photon level [10,14], we provide a comprehensive analysis of the impact of pure dephasing and phonon scattering on cavity feeding and the copolarization effect in the weak-coupling regime.

The QD-cavity system employed consists of a single InGaAs/GaAs pyramidal QD [15] aligned with the intensity maximum of the CM of a modified photonic crystal (PhC) $L3$ membrane cavity [Figs. 1(b) and 1(c)]. The QDs were grown on a 265 nm thick (111)B GaAs membrane substrate patterned with inverted pyramidal recesses, defined using e-beam lithography and wet chemical etching. The InGaAs/GaAs QDs were grown by metalorganic vapor phase epitaxy, nucleating at the apex of the inverted pyramids without the formation of a 2D wetting layer. The 200 nm-pitch PhC hole patterns were written and properly aligned with the QD positions (alignment precision ≤ 50 nm) using e-beam lithography and etched by induced coupled plasma etching. The resulting structure consists of a single pyramidal QD in the center of a modified-$L3$ cavity [16]. PL measurements of the QD-cavity systems were performed in a He-flow cryostat by continuous wave (cw) photoexcitation using a focused Ti-sapphire laser beam (~ 1 μm spot, 730 nm wavelength) with ~ 80 μeV spectral resolution. Polarization-resolved spectra were acquired using a $\lambda/2$ wave plate followed by a linear polarizer placed in the detection path.

The QD PL spectra are reproducible, exhibiting transitions of the neutral exciton (X), the biexciton ($2X$), and the negatively charged exciton (X^-) [14]. In two selected samples, QD1 and QD2, the CM is tuned near the X^- line, showing typical CM off-resonant emission and copolarization of the excitonic transition with the CM transition [Figs. 1(d) and 1(e)]. The copolarization effect is quantified by the displayed spectra of the degree of linear polarization DOLP $= (I_V - I_H)/(I_V + I_H)$. The difference in (Lorentzian) full width at half maximum (FWHM) of the CM ($\kappa_1 = 590$ μeV and $\kappa_2 = 440$ μeV) and exciton line ($\Gamma_1 = 450$ μeV and $\Gamma_2 = 200$ μeV) stems from variations in cavity Q-factor and exciton dephasing from sample to sample. Since the binding energies (with respect to X) of X^- and $2X$ in these dots are ~ 5 meV and < 1 meV [14], respectively, this system well represents an isolated QD transition coupled to a CM. The absence of fine structure splitting for the X^- transition [17,18] further facilitates interpretation of the observations. Figures 1(d) and 1(e) demonstrate two different signatures of QD-cavity coupling: off-resonant cavity feeding, specific to solid-state systems, and QD-CM copolarization of emission.

The fact that the X^- transition is spectrally shifted by at least 4 meV from the other excitonic transitions allows us to consider a model based on a TLS [Fig. 2(a)], with Bohr frequency $[\omega_0/(2\pi)]$ coupled to a CM at frequency $[\omega_{\mathrm{cav}}/(2\pi)]$, with a detuning energy of $\hbar\delta = \hbar\omega_0 - \hbar\omega_{\mathrm{cav}}$. The X^- transition is represented by a randomly oriented TLS [Fig. 2(a)]. The TLS-CM coupling is described in the

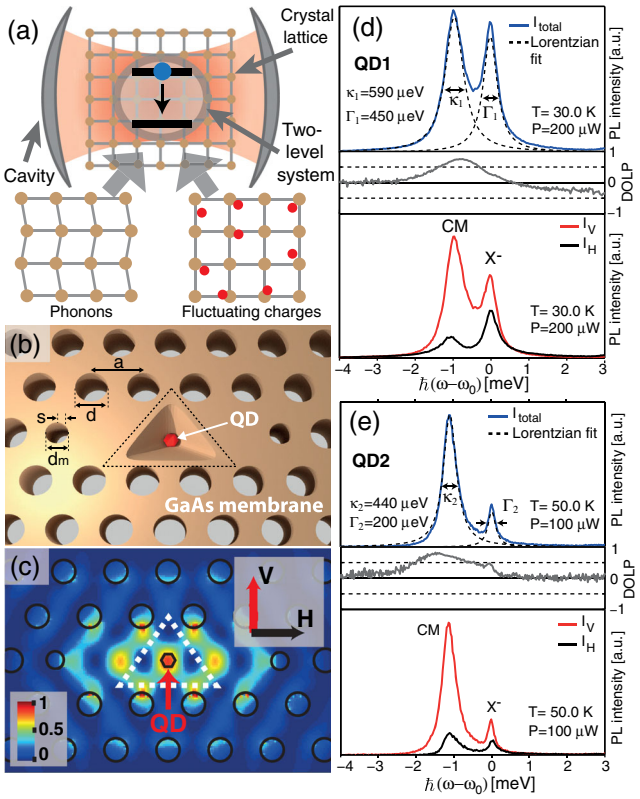

FIG. 1. QD-cavity system investigated. (a) Schematic illustration of the system. (b) Schematic of the QD positioned at the center of a modified-$L3$ PhC cavity: $a = 200$ nm, $d = 130$ nm, $d_m = 110$ nm, and $s = 30$ nm. (c) Computed field intensity distribution of the fundamental CM. (d) [(e)] (Top panel) PL spectrum of QD1 (QD2) coupled to the fundamental CM. Lorentzian fits (the dashed lines) yield the linewidths κ and Γ of, respectively, the CM and X^- transitions. (Bottom panel) PL spectrum resolved in linear polarization along the vertical (V) and horizontal (H) directions indicated in (c). (Center panel) Degree of linear polarization of the PL.

Lindblad master equation formalism [19,20] using the Jaynes-Cummings Hamiltonian in the rotating wave approximation (see the Supplemental Material, method A for details [21]). TLS and cavity losses at rates γ and κ, respectively, are modeled by the jump operators $L_\gamma = \sqrt{\gamma}\sigma^-$ and $L_\kappa = \sqrt{\kappa}a$ and incoherent pumping of the TLS is added through the Lindblad term $L_P = \sqrt{P}\sigma^+$, with a and σ^- being the annihilation operators of the CM and the TLS, respectively, and $\sigma^+ = (\sigma^-)^\dagger$. Pure dephasing caused by fluctuating electrical charges near the QD is modeled by the Lindblad term [19] $L_{\gamma_d} = \sqrt{(\gamma_d/4)}\sigma^z$, with γ_d being the dephasing rate and $\sigma^z = 2\sigma^+\sigma^- - 1$, leading to a Lorentzian broadening of the line's FWHM by γ_d. Phonon scattering is described by the Lindblad term [25]

$$L_{\mathrm{ph}} = \sqrt{\Gamma^{\mathrm{ph}}(\delta)}a^\dagger\sigma^- \tag{1}$$

that accounts for the phonon-induced transfer of excitations from the QD exciton to the energy mismatched CM. Depending on the sign of the detuning, the annihilation of a QD exciton and the creation of a cavity photon requires the absorption ($\delta < 0$) or emission ($\delta > 0$) of a phonon, resulting in an asymmetry of the phonon scattering rate $\Gamma^{\mathrm{ph}}(\delta)$ with respect to detuning. Whereas γ, κ, and γ_d can be inferred from time-resolved and spectral measurements, no indication of the effective phonon scattering rate $\Gamma^{\mathrm{ph}}(\delta)$ is readily available. However, it can be estimated using a microscopic model for the electron-phonon interaction [25,26] (see the Supplemental Material, method B [21]):

$$\Gamma^{\mathrm{ph}}(\delta) = \frac{2\pi}{\hbar^2}\left(\frac{g\cos(\theta)}{\delta}\right)^2 d(\delta), \tag{2}$$

where g is the TLS-cavity coupling strength and θ the angle between the QD dipole and the CM electric field at the position of the QD. $d(\delta)$ is the effective phonon density of states [26,27] given by

$$d(\delta) = A\delta^2[n(\delta,T) - n(-\delta,T) + 1] \times \exp\left(-\frac{\delta^2\ell^2}{2c_s^2}\right)\frac{\mathrm{erf}\left(\frac{\delta}{c_s}\sqrt{\frac{\ell_z^2-\ell^2}{2}}\right)}{\sqrt{\frac{(\ell_z^2-\ell^2)}{2}}}, \tag{3}$$

where $n(\delta,T)$ is the Bose-Einstein distribution at temperature T and A a constant depending on the speed of sound in the material c_s, the material's mass density, and the deformation potential. ℓ and ℓ_z are the Gaussian standard deviations of in-plane and out-of-plane exciton electronic wave functions.

Numerically solving the master equation yields the steady-state power spectra for the TLS (S^θ_{TLS}) and cavity mode (S^θ_{cav}) emissions through the Wiener-Khintchine theorem [28] (see the Supplemental Material, method C for details [21]). Following Auffèves *et al.* [29], we computed the following quantities:

$$N^\theta_{\mathrm{TLS}}(\omega) = |F_{\mathrm{at}}|^2\gamma S^\theta_{\mathrm{TLS}}(\omega) \tag{4}$$

and

$$N^\theta_{\mathrm{cav}}(\omega) = |F_{\mathrm{cav}}|^2\kappa S^\theta_{\mathrm{cav}}(\omega), \tag{5}$$

which can be directly compared to the measured PL spectra. The total vertically and horizontally polarized collected spectra are written

$$N^V_{\mathrm{total}}(\omega) = \sum_\theta [N^\theta_{\mathrm{cav}}(\omega) + \cos(\theta)^2 N^\theta_{\mathrm{TLS}}(\omega) + \cos(\theta)F^*_{\mathrm{cav}}F_{\mathrm{TLS}}\sqrt{\kappa\gamma}S^\theta_{\mathrm{cav;TLS}}(\omega) + \cos(\theta)F^*_{\mathrm{TLS}}F_{\mathrm{cav}}\sqrt{\gamma\kappa}S^\theta_{\mathrm{TLS;cav}}(\omega)] \tag{6}$$

and

$$N^H_{\mathrm{total}}(\omega) = \sum_\theta \sin(\theta)^2 N^\theta_{\mathrm{TLS}}(\omega), \tag{7}$$

with

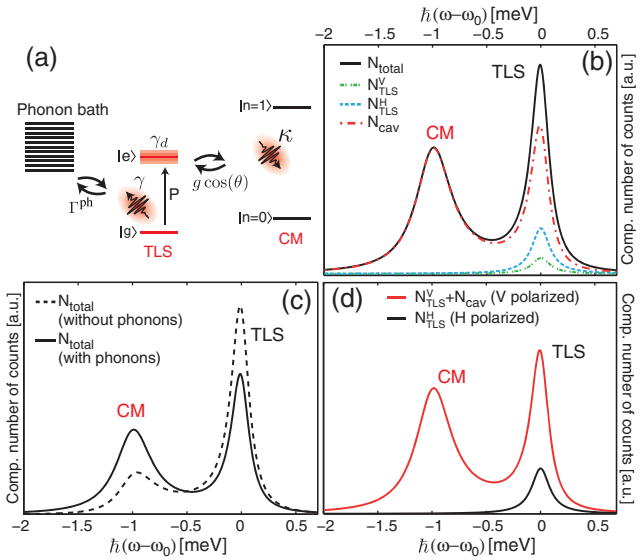

FIG. 2. Model of QD-cavity interactions. (a) Schematic of the model describing the TLS-cavity system. The decay rates of the TLS and the cavity mode are γ and κ, respectively. The coupling strength between the TLS and the CM is $g\cos(\theta)$. The TLS pure dephasing rate is γ_d and the TLS-phonon bath coupling strength is g_{ph}. (b) Computed PL spectrum showing the contributions of the vertical (V) and horizontal (H) components of the TLS and the CM (see the text for parameter values). (c) PL spectra with the same simulation parameters as in (b), with (solid line) and without (dashed line) TLS-phonon interactions. (d) Computed PL spectrum linearly resolved in polarization along the directions indicated in Fig. 1(a) [with the same simulation parameters as in (b)].

$$N_{\mathrm{total}} = N^{V}_{\mathrm{total}}(\omega) + N^{H}_{\mathrm{total}}(\omega), \tag{8}$$

where the coefficients F_{at} and F_{cav} describe coupling efficiencies to the photon detector and relative phases of the TLS and cavity mode decay channels, respectively, and the last two terms of the sum in Eq. (6) account for the interferences between the TLS and cavity decay channels [30,31]. We find that these interference terms do not modify the qualitative conclusions of our study and thus neglect them in the rest of this Letter. Because of the high in-plane symmetry of pyramidal QDs [32], we assume a random orientation of the exciton dipole in the growth plane. Since the QD lifetime is much smaller than the integration time used to acquire the experimental spectra in cw mode excitation, we average over all possible orientations of the QD exciton dipole. To account for this in the simulations, we take the sum on θ in Eqs. (6) and (7).

Figure 2(b) shows the computed spectra $N_{\mathrm{total}}(\omega)$, $N_{\mathrm{cav}}(\omega)$, $N^{V}_{\mathrm{TLS}}(\omega) = \sum_\theta \cos(\theta)^2 N^{\theta}_{\mathrm{TLS}}(\omega)$, and $N^{H}_{\mathrm{TLS}}(\omega) = \sum_\theta \sin(\theta)^2 N^{\theta}_{\mathrm{TLS}}(\omega)$ for the following simulation parameters: $\hbar\delta = 1$ meV, $\hbar\kappa = 400$ μeV, $\hbar\gamma = 0.2$ μeV, $\hbar\gamma_d = 200$ μeV, $\hbar g = 50$ μeV, $(2\pi/\hbar^2)A = 0.8$ nm/meV, $T = 10$ K, $\hbar P = 0.1$ μeV, $\ell = 4$ nm, $\ell_z = 2$ nm, $F_{\mathrm{cav}} = 0.4$, and $F_{\mathrm{at}} = 0.3$. The finite coupling between the TLS and the CM yields emission by the cavity channel at the TLS transition energy and reduction of the V-polarized TLS emission. Figure 2(c) shows $N_{\mathrm{total}}(\omega)$ without ($A = 0$) and with ($(2\pi/\hbar^2)A = 0.8$ nm/meV) phonon scattering, illustrating the cavity feeding by the TLS transition induced by phonon scattering [other parameters are as in Fig. 2(b)]. Resolution of the emission spectra into V and H components [Fig. 2(d)] illustrates the copolarization of the TLS transition induced by the finite coupling of the TLS to the CM.

The evolution of the copolarization and cavity feeding effects with QD-CM detuning is displayed in Fig. 3, where polarization-resolved PL spectra of QD1 and QD2 [Fig. 3(a) and 3(c)] are compared to the fitted computed spectra [Figs. 3(b) and 3(d)]. The normalized, measured spectra span a detuning range of about ± 3 meV induced by the temperature dependent (In)GaAs band gap. The energy shifts of the CM and X^- transitions as a function of temperature are shown in the Supplemental Material, Figs. S3(a)–S3(d). Unlike in recent reports [33,34], frequency cavity pulling effects are not visible in the experimental data (see the Supplemental Material, Sec. D for details [21]). The fitting parameters are listed in Table I. γ_d and κ were retrieved from the fits of Figs. 1(d) and 1(e). γ, the intrinsic QD linewidth in the PhC band gap, was obtained from time-resolved measurements performed on nominally identical pyramidal QDs inside the photonic crystal band gap and corresponds to a lifetime of 3 ns. F_{cav} and F_{at} were computed using 3D finite-difference time domain simulations. The values used for ℓ and ℓ_z are

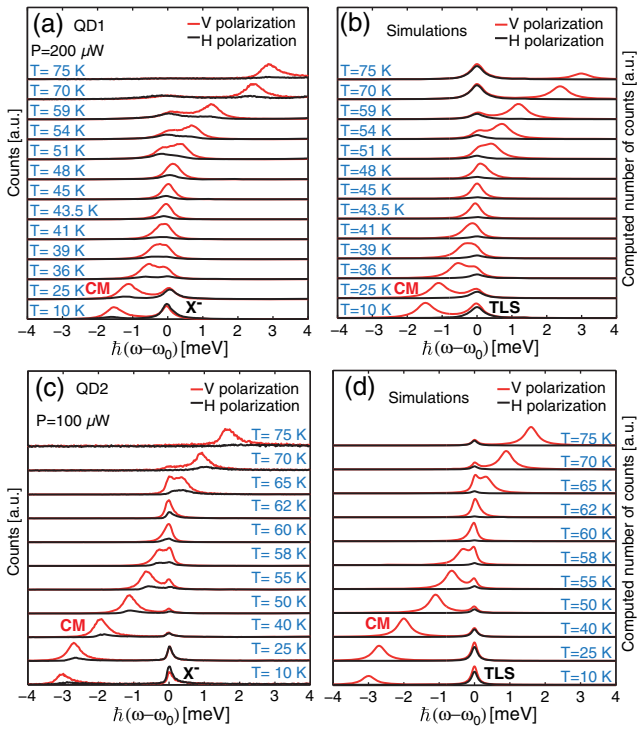

FIG. 3. Comparing experiments and modeling. Experimental (a) and simulated (b) temperature dependent PL spectra of the cavity-QD systems, linearly resolved in polarization along the directions indicated in Fig. 1(c) for QD1. (c),(d) The same for QD2.

suitable for InGaAs QDs with confinement dimensions of 10 nm in plane and 5 nm in the growth direction. The remaining three parameters (g, A, and P) were adjusted to fit the experimental data. The results of the modeling reproduce remarkably well the QD-cavity spectral detuning dynamics for both structures up to $T \sim 65$ K. The discrepancies at higher temperatures are attributed to nonradiative recombination such as thermally activated nonradiative recombination in barriers [35] and thermally induced escape of carriers [36].

Efficient CM feeding by the TLS system occurs throughout the ± 3 meV detuning range scanned. Narrowing of the CM linewidths [34] for small detunings was observed in the experimental data and the simulations as shown in the Supplemental Material, Fig. S3(f) [21]. Near resonance, the luminescence at the QD transition energy is a superposition of photons escaping through the QD and CM decay channels. In the "bad cavity" regime ($\kappa \gg \gamma$), cavity photons are emitted at a faster rate than QD photons, which translates here into an increase of the emission intensity at the X^- energy. This increase of the X^- integrated intensity with decreasing detuning reaches tenfold enhancement at resonance and is qualitatively reproduced by the simulations as shown in the Supplemental Material, Fig. S3(e) [21]. Polarizationwise, the additional cavity photons emitted at the energy of the QD transition are V polarized. This explains the gradual copolarization of the X^- transition with decreasing detuning, which is well reproduced by the modeling. Whereas off-resonant CM emission is observed for detuning as large as ± 3 meV, copolarization of the X^- transition is visible only for detuning as large as ± 1 meV, in agreement with previous reports [10]. This behavior is well accounted for by the model, showing that copolarization persists only when the CM and X^- lines significantly overlap. We note that measurements were performed below QD saturation, without background emission in the vicinity of the s-state transitions. From this fitting procedure, we were able to extract coupling strengths of $\hbar g = 20$ μeV for QD1 and $\hbar g = 50$ μeV for QD2 (see Table I). These values are in line with those reported for InGaAs/GaAs QDs [37–39]. Given our deterministic positioning of the QD at a maximum of the CM intensity, these values mainly reflect the degree of mutual alignment of the electric field of the mode and the QD dipole moment, rather than the nonoptimal overlap of the CM intensity with the QD.

The more general features of the cavity feeding and CM-exciton copolarization are presented in the maps of Fig. 4. Figure 4(b) shows the calculated relative intensity of the CM peak $I_{\mathrm{CM}}/(I_{\mathrm{CM}} + I_{\mathrm{TLS}})$ as a function of detuning and QD-cavity coupling strength. The relative CM peak intensity reaches a maximum for detunings of 1.7 meV and increases with g. The detunings for which the maximum CM relative intensity is reached correspond to the energies of longitudinal acoustic phonons interacting with QD excitons having a localization length of 4 nm [6], indicating

TABLE I. Table of parameters used for the simulations of Figs. 3(b) and 3(d).

Parameter	Symbol (unit)	QD1	QD2
TLS loss rate	$\hbar\gamma(\mu\mathrm{eV})$	0.2	
CM loss rate	$\hbar\kappa(\mu\mathrm{eV})$	590	440
Pure dephasing rate	$\hbar\gamma_d(\mu\mathrm{eV})$	450	200
TLS-CM coupling strength	$\hbar g(\mu\mathrm{eV})$	20	50
Phonon density of state constant	$(2\pi/\hbar^2)A(\mathrm{nm/meV})$	1.3	1.4
Incoherent pumping rate	$\hbar P(\mathrm{neV})$	10	5
Wave function standard deviation (in plane)	$\ell(\mathrm{nm})$	4	
Wave function standard deviation (vertical)	$\ell_z(\mathrm{nm})$	2	
CM coupling efficiency to detector	F_{cav}	0.4	
TLS coupling efficiency to detector	F_{at}	0.3	

that phonon scattering is responsible for this strong increase of the off-resonant CM emission. Note that, although not investigated here, phonon scattering also influences the QD decay rate [27,40]. The decrease in relative CM emission for detunings < 1.7 meV is in agreement with our measurements and other reports [41]. Figure 4(c) displays the TLS peak DOLP as a function of detuning and sample temperature. Below $T = 50$ K, the DOLP is always positive and is maximum for small QD-cavity detunings. Above $T = 50$ K, a region of negative DOLP appears for QD-cavity detunings between ~ 1 and 3 meV, a direct

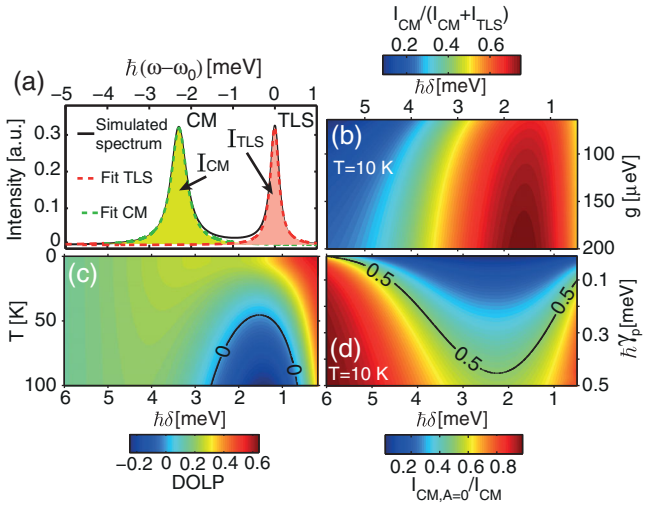

FIG. 4. Further model predictions. (a) Simulated spectrum with simulation parameters as in Fig. 3 for QD2, except that $\hbar g = 105$ μeV. Peak integrated intensities evaluated using Lorentzian line shapes I_{CM} and I_{TLS}. (b) Relative CM peak intensity versus g and TLS-CM detunings. (c) TLS peak DOLP versus temperature and TLS-CM detuning. (d) Intensity of the CM peak without phonon scattering $I_{\mathrm{CM},A=0}$ relative to I_{CM} including phonon scattering versus γ_p and TLS-CM detunings. The simulation parameters correspond to QD2.

consequence of the increase in efficiency of phonon mediated cavity feeding with temperature, which leads to a depletion of the V-polarized TLS emission. Figure 4(d) presents the intensity of the CM peak without phonon scattering $I_{\mathrm{CM},A=0}$, where the only decoherence mechanism is pure dephasing, relative to I_{CM}, which includes phonon scattering. The line in Fig. 4(d) corresponding to a ratio $I_{\mathrm{CM},A=0}/I_{\mathrm{CM}} = 0.5$ demarcates two regions of parameters for which either pure dephasing or phonon scattering contributes the most to the off-resonant CM emission. It is interesting to note that, for certain pure dephasing rates, both regions can be probed by changing only the QD-cavity detuning. An analysis of the relative contribution of dephasing and phonon scattering for QD1 and QD2 is given in the Supplemental Material, Fig. S4 [21].

In conclusion, using a TLS-like QD system embedded in a solid-state environment coupled with a single mode photonic cavity, we elucidated the roles of phonons and pure dephasing on exciton-cavity interaction in the weak-coupling regime. In contrast to previous studies performed with self-assembled QDs, the absence of spurious multi-excitonic effects in pyramidal QDs allowed a quantitative analysis of the effects of phonon scattering and pure dephasing on off-resonant CM emission. Besides providing insight into weak-coupling mechanisms in solid-state c-QED phenomena, the results yield useful information for designing integrated quantum photonic systems such as efficient single photon sources.

This work was supported by the Swiss National Science Foundation.

*clement.jarlov@epfl.ch

[1] P. Goy, J. M. Raimond, M. Gross, and S. Haroche, Phys. Rev. Lett. **50**, 1903 (1983).

[2] A. Blais, R.-S. Huang, A. Wallraff, S. M. Girvin, and R. J. Schoelkopf, Phys. Rev. A **69**, 062320 (2004).

[3] A. Imamoglu, Opt. Photonics News **13**, 22 (2002).

[4] C. Piermarocchi, P. Chen, L. J. Sham, and D. G. Steel, Phys. Rev. Lett. **89**, 167402 (2002).

[5] E. Pazy, E. Biolatti, T. Calarco, I. D'Amico, P. Zanardi, F. Rossi, and P. Zoller, Europhys. Lett. **62**, 175 (2003).

[6] L. Besombes, K. Kheng, L. Marsal, and H. Mariette, Phys. Rev. B **63**, 155307 (2001).

[7] A. Auffèves, J.-M. Gérard, and J.-P. Poizat, Phys. Rev. A **79**, 053838 (2009).

[8] M. Winger, T. Volz, G. Tarel, S. Portolan, A. Badolato, K. J. Hennessy, E. L. Hu, A. Beveratos, J. Finley, V. Savona, and A. Imamoğlu, Phys. Rev. Lett. **103**, 207403 (2009).

[9] M. Settnes, P. Kaer, A. Moelbjerg, and J. Mork, Phys. Rev. Lett. **111**, 067403 (2013).

[10] M. Calic, P. Gallo, M. Felici, K. A. Atlasov, B. Dwir, A. Rudra, G. Biasiol, L. Sorba, G. Tarel, V. Savona, and E. Kapon, Phys. Rev. Lett. **106**, 227402 (2011).

[11] C. Jarlov, A. Lyasota, L. Ferrier, P. Gallo, B. Dwir, A. Rudra, and E. Kapon, Appl. Phys. Lett. **107**, 191101 (2015).

[12] J. Suffczyński, A. Dousse, K. Gauthron, A. Lemaître, I. Sagnes, L. Lanco, J. Bloch, P. Voisin, and P. Senellart, Phys. Rev. Lett. **103**, 027401 (2009).

[13] E. Gallardo, L. J. Martínez, A. K. Nowak, H. P. van der Meulen, J. M. Calleja, C. Tejedor, I. Prieto, D. Granados, A. G. Taboada, J. M. García, and P. A. Postigo, Opt. Express **18**, 13301 (2010).

[14] C. Jarlov, P. Gallo, M. Calic, B. Dwir, A. Rudra, and E. Kapon,Appl. Phys. Lett. **101**, 191101 (2012).

[15] M. Felici, P. Gallo, A. Mohan, B. Dwir, A. Rudra, and E. Kapon, Small **5**, 938 (2009).

[16] P. Gallo, M. Felici, B. Dwir, K. A. Atlasov, K. F. Karlsson, A. Rudra, A. Mohan, G. Biasiol, L. Sorba, and E. Kapon, Appl. Phys. Lett. **92**, 263101 (2008).

[17] M. Bayer, G. Ortner, O. Stern, A. Kuther, A. A. Gorbunov, A. Forchel, P. Hawrylak, S. Fafard, K. Hinzer, T. L. Reinecke, S. N. Walck, J. P. Reithmaier, F. Klopf, and F. Schäfer, Phys. Rev. B **65**, 195315 (2002).

[18] J. G. Tischler, A. S. Bracker, D. Gammon, and D. Park, Phys. Rev. B **66**, 081310 (2002).

[19] A. Auffèves, D. Gerace, J.-M. Gérard, M. F. Santos, L. C. Andreani, and J.-P. Poizat, Phys. Rev. B **81**, 245419 (2010).

[20] A. Majumdar, E. D. Kim, Y. Gong, M. Bajcsy, and J. Vučković, Phys. Rev. B **84**, 085309 (2011).

[21] See Supplemental Material at http://link.aps.org/supplemental/10.1103/PhysRevLett.117.076801, which includes Refs. [22–24], for additional information on the Jaynes-Cummings model [method A], phonon scattering rate calculations [method B] and numerical resolution of the master equation [method C]. Additional experimental and simulated data complementing the results of Fig. 3 are presented in sections D and E.

[22] K. P. O'Donnell and X. Chen, Appl. Phys. Lett. **58**, 2924 (1991).

[23] G. Ortner, M. Schwab, M. Bayer, R. Pässler, S. Fafard, Z. Wasilewski, P. Hawrylak, and A. Forchel, Phys. Rev. B **72**, 085328 (2005).

[24] N. Cherroret, A. Chakravarty, and A. Kar, J. Mater. Sci. **43**, 1795 (2008).

[25] U. Hohenester, Phys. Rev. B **81**, 155303 (2010).

[26] P. Kaer, T. R. Nielsen, P. Lodahl, A.-P. Jauho, and J. Mørk, Phys. Rev. B **86**, 085302 (2012).

[27] K. H. Madsen, P. Kaer, A. Kreiner-Møller, S. Stobbe, A. Nysteen, J. Mørk, and P. Lodahl, Phys. Rev. B **88**, 045316 (2013).

[28] J. R. Johansson, P. D. Nation, and F. Nori, Comput. Phys. Commun. **183**, 1760 (2012).

[29] A. Auffèves, B. Besga, J.-M. Gérard, and J.-P. Poizat, Phys. Rev. A **77**, 063833 (2008).

[30] K. H. Madsen and P. Lodahl, New J. Phys. **15**, 025013 (2013).

[31] Y. Ota, R. Ohta, N. Kumagai, S. Iwamoto, and Y. Arakawa, Phys. Rev. Lett. **114**, 143603 (2015).

[32] K. F. Karlsson, V. Troncale, D. Y. Oberli, A. Malko, E. Pelucchi, A. Rudra, and E. Kapon, Appl. Phys. Lett. **89**, 251113 (2006).

[33] T. Tawara, H. Kamada, T. Tanabe, T. Sogawa, H. Okamoto, P. Yao, P. K. Pathak, and S. Hughes, Opt. Express **18**, 2719 (2010).

[34] D. Valente, J. Suffczyński, T. Jakubczyk, A. Dousse, A. Lemaître, I. Sagnes, L. Lanco, P. Voisin, A. Auffèves, and P. Senellart, Phys. Rev. B **89**, 041302 (2014).

[35] R. Heitz, I. Mukhametzhanov, A. Madhukar, A. Hoffmann, and D. Bimberg, J. Electron. Mater. **28**, 520 (1999).

[36] P. Bhattacharya, K. Kamath, J. Singh, D. Klotzkin, J. Phillips, H.-T. Jiang, N. Chervela, T. Norris, T. Sosnowski, J. Laskar, and M. Ramana Murty, IEEE Trans. Electron Devices **46**, 871 (1999).

[37] J. P. Reithmaier, G. Sęk, A. Löffler, C. Hofmann, S. Kuhn, S. Reitzenstein, L. V. Keldysh, V. D. Kulakovskii, T. L. Reinecke, and A. Forchel, Nature (London) **432**, 197 (2004).

[38] K. Hennessy, A. Badolato, M. Winger, D. Gerace, M. Atatüre, S. Gulde, S. Fält, E. L. Hu, and A. Imamoğlu, Nature (London) **445**, 896 (2007).

[39] S. Münch, S. Reitzenstein, P. Franeck, A. Löffler, T. Heindel, S. Höfling, L. Worschech, and A. Forchel, Opt. Express **17**, 12821 (2009).

[40] S. L. Portalupi, G. Hornecker, V. Giesz, T. Grange, A. Lemaître, J. Demory, I. Sagnes, N. D. Lanzillotti-Kimura, L. Lanco, A. Auffèves, and P. Senellart, Nano Lett. **15**, 6290 (2015).

[41] S. Ates, S. M. Ulrich, A. Ulhaq, S. Reitzenstein, A. Löffler, S. Höfling, A. Forchel, and P. Michler, Nat. Photonics **3**, 724 (2009).